CrossMark

J. Fluid Mech. (2019), *vol.* 873, *pp.* 816–834. © Cambridge University Press 2019
doi:10.1017/jfm.2019.426

Confinements regulate capillary instabilities of fluid threads

Xiaodong Chen[1], Chundong Xue[3,4] and Guoqing Hu[2,3,4,†,‡]

[1]School of Aerospace Engineering, Beijing Institute of Technology, Beijing 100081, China

[2]Department of Engineering Mechanics, Zhejiang University, Hangzhou 310027, China

[3]State Key Laboratory of Nonlinear Mechanics, Institute of Mechanics, Chinese Academy of Sciences, Beijing 100190, China

[4]School of Engineering Science, University of Chinese Academy of Sciences, Beijing 100049, China

(Received 13 December 2018; revised 21 May 2019; accepted 22 May 2019;
first published online 28 June 2019)

We study the breakup of confined fluid threads at low flow rates to understand instability mechanisms. To determine the critical conditions between the earlier quasi-stable necking stage and the later unstable collapse stage, simulations and experiments are designed to operate at an extremely low flow rate. The critical mean radii at the neck centres are identified by the stop-flow method for elementary microfluidic configurations. Two distinct origins of capillary instabilities are revealed for different confinement situations. One is the gradient of capillary pressure induced by the confinements of geometry and external flow, whereas the other is the competition between the capillary pressure and internal pressure determined by the confinements.

Key words: breakup/coalescence, microfluidics, multiphase flow

1. Introduction

Fluid thread breakup is a widespread phenomenon in nature, industry, and daily life (Eggers *et al.* 2007; Bhat *et al.* 2010; van Hoeve *et al.* 2010; Tagawa *et al.* 2012). As a common example, columnar water jets from a showerhead are unstable downstream of the nozzles and break into droplets in air. This breakup scenario is called Rayleigh–Plateau (R–P) instability (Plateau 1873; Rayleigh 1878), which is also called capillary instability at low flow rates where the driving force is interfacial tension (Eggers *et al.* 2007; Eggers & Villermaux 2008). In contrast, a fluid thread covered by a thin film of another fluid within a tube can be stable (Duclaux, Clanet & Quere 2006). For instance, a long air bubble in an intravenous line maintains its shape while moving slowly with the liquid. This type of tightly confined fluid thread is often encountered in various processes, including pore-scale breakup in enhanced oil recovery (Olbricht 1996) and droplet or bubble generation in microfluidic devices (Squires & Quake 2005; Anna 2016), where confined fluid threads are squeezed into fluid necks at channel junctions and eventually break into microdroplets. The interface

† Email addresses for correspondence: ghu@zju.edu.cn, guoqing.hu@imech.ac.cn

‡ The original version of this article was published with an incorrect author name. A notice detailing this has been published and the error rectified in the online and print PDF and HTML copies.

https://doi.org/10.1017/jfm.2019.426 Published online by Cambridge University Press

is quasi-stable in the earlier necking stage and becomes unstable in the later collapse stage (Garstecki, Stone & Whitesides 2005). The stage transition is thought to be an R–P instability (Link *et al.* 2004; Garstecki *et al.* 2005; De Menech *et al.* 2008) or initiated not by an R–P instability but rather by a reversed flow from the thread tip to the neck (van Steijn, Kleijn & Kreutzer 2009). The mechanisms of the onset of interfacial instabilities are still puzzling.

Here, through newly designed numerical simulations and experiments at extremely low capillary numbers, we identify the transitions between the quasi-stable and unstable stages for confined fluid threads. Two breakup mechanisms are uncovered for different confinement situations in surprisingly simple terms.

2. Numerical and experimental methods

Numerical simulations are conducted using the Gerris flow solver (http://gfs.sf.net). Combining an adaptive quad/octree spatial discretization, geometrical volume-of-fluid interface representation, balanced-force continuum-surface-force surface tension formulation, and height-function curvature estimation, the method is shown to recover exact equilibrium (to machine accuracy) between surface tension and pressure gradient in the case of a stationary droplet, irrespective of viscosity and spatial resolution (Popinet 2009). The accuracy of the code has been validated in our previous studies for various interfacial flow problems (Chen *et al.* 2013, 2014). The motion of the fluid thread inside the continuous phase forms a thin lubrication film between the fluid thread and the channel wall (Taylor 1961). The ratio of the film thickness to the channel diameter was found to scale with $Ca^{2/3}$ (Bretherton 1961), where Ca is the capillary number. A thickness-based refinement criterion developed in the previous work (Chen & Yang 2014) is used to resolve the film by at least two meshes in thickness direction. However, when $Ca \sim 10^{-6}$, the ratio of the film thickness to the channel diameter is in the order of 10^{-4}. It is too costly to resolve such a film that plays only a minor role in determining the shape of the fluid thread. In practice, the film may vanish, and the interface may make contact with the wall under such a small Ca. Therefore, the film is not resolved for cases under $Ca \sim 10^{-6}$, while a contact angle of 180° is set on the wall to make it fully hydrophobic. A curvature-based refinement criterion (Popinet 2009) is also applied to increase the grid resolution according to the thinning of the neck region during breakup. The breakup dynamics of confined fluid threads in various microfluidic configurations are considered in this paper. The geometry and boundary conditions will be described when mentioned. Grid independence studies are carried out for each configuration to obtain the proper interfacial mesh size to capture the breakup dynamics.

Experiments are performed in circular microchannels that are fabricated by a rapid prototyping method (Ghorbanian, Qasaimeh & Juncker 2010). Iron wires are cut and arranged on a cured polydimethylsiloxane (PDMS) flat piece. Wires are connected by dropping a small amount of melted paraffin into the gaps between the wires. The connected wires are then covered with the uncured PDMS. After the PDMS is cured, the wires are pulled out to form the desired configurations. To obtain a hydrophobic surface, the microchannels are filled with Rain-X® rain repellent and then washed with deionized water. The hydrophobic treatment also improves the sharpness of the interface during high-speed imaging. The openings of the microchannels are connected with plastic tubes to form microfluidic devices. The microfluidic device is mounted on the stage of an inverted microscope (Nikon Eclipse Ti, Japan). Fluids are introduced into the channel using syringe pumps (Pump 11 Elite, Harvard Apparatus

https://doi.org/10.1017/jfm.2019.426 Published online by Cambridge University Press

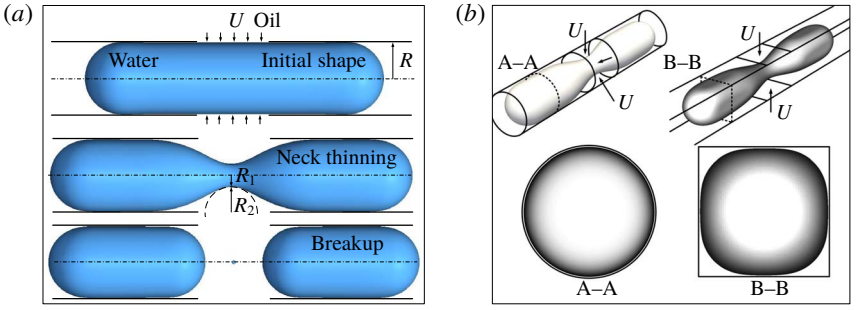


FIGURE 1. (Colour online) Axisymmetric breakup of a confined fluid thread. (*a*) Sketch of the breakup process. (*b*) Comparison of droplet shapes in channels with circular and rectangular cross-sections during breakup.

Inc., USA). Breakup dynamics in the microchannel is recorded using a Phantom v7.3 high-speed camera (Vision Research Inc., USA) and Phantom Camera Control software. Photographs of the microfluidic devices can be found in the supplementary material available at https://doi.org/10.1017/jfm.2019.426.

3. Results and discussion

3.1. *Critical mean neck radius for the axisymmetric breakup*

Inspired by the axisymmetric configurations used in studying the breakup mechanism of unbounded fluid threads (Gordillo *et al.* 2005; Eggers *et al.* 2007), we first investigate the breakup of an axisymmetric water thread that is tightly confined inside a circular microchannel, as shown in figure 1(*a*). A fluid neck forms under the squeezing of the oil side flow and then collapses. As illustrated in figure 1(*b*), a circular channel avoids the empty corners found in a rectangular channel through which oil inevitably flows causing leakage and making it difficult to deform the interface under low flow rates (Dollet *et al.* 2008; Shui *et al.* 2008). Using circular channels, we can overcome the leakage problem and study the breakup at extremely low flow rates. A water droplet (viscosity $\mu_w = 1$ mPa s, density $\rho_w = 998$ kg m^{-3}) is initially tightly confined in a circular microchannel with radius $R = 25$ μm. The initial shape of the droplet is a cylinder with two hemispherical tips. The incoming oil (viscosity $\mu_o = 8$ mPa s, density $\rho_o = 770$ kg m^{-3}) from the lateral opening (width of 50 μm) with a velocity of U deforms the interface (interfacial tension $\sigma = 5$ mN m^{-1}). A two-dimensional axisymmetric model is established to consider only a quarter of the cross-section of the configuration due to the axial and bilateral symmetries (figure S2(*a*) in the supplementary material). This simplification allows us to simulate the axisymmetric breakup efficiently and accurately for a wide range of small capillary numbers, $Ca = \mu_w U/\sigma$.

To provide intuitive insights into the breakup dynamics, photorealistic ray-tracing rendering is performed to show the breakup dynamics using the POV-Ray software (Persistence of Vision Pty. Ltd 2013). Figure 2 shows three series of images leading to the final collapse under three Ca values varying from 2.0×10^{-5} to 2.0×10^{-3}. Thickness-based and curvature-based refinements allow us to obtain the detailed flow dynamics at the lubrication film near the channel wall, and the final collapse that leads

https://doi.org/10.1017/jfm.2019.426 Published online by Cambridge University Press

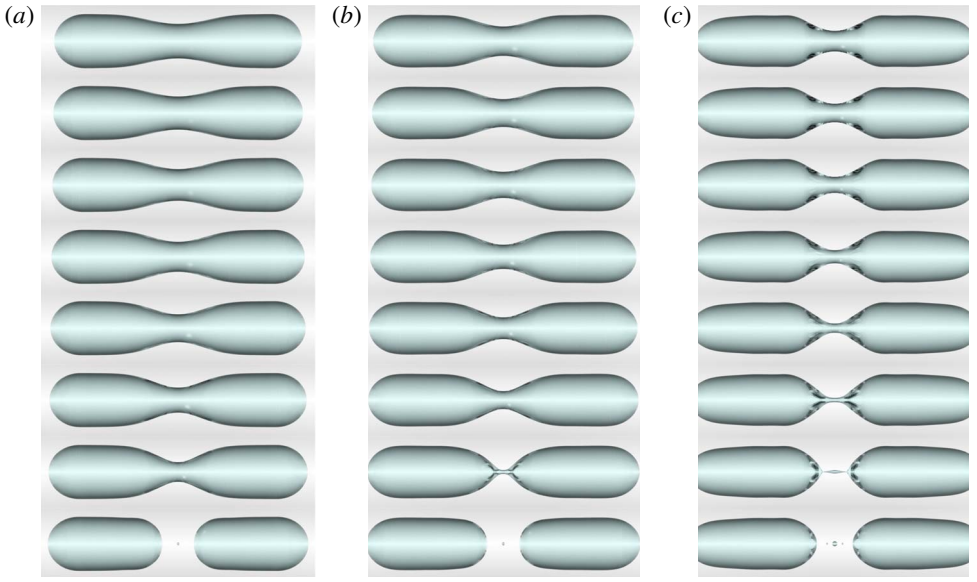


FIGURE 2. (Colour online) Time evolutions of the axisymmetric breakup of a confined fluid thread with photorealistic ray-tracing rendering under different Ca of 2.0×10^{-5} (a), 2.0×10^{-4} (b) and 2.0×10^{-3} (c). The time interval is constant for each series.

to the generation of satellite droplets at the neck centre, respectively. The two ends of the fluid thread are hemispherical under $Ca = 2.0 \times 10^{-5}$ (figure 2a) and 2.0×10^{-4} (figure 2b), but have a bullet-like shape under $Ca = 2.0 \times 10^{-3}$ (figure 2c). The breakup dynamics under $Ca = 2.0 \times 10^{-3}$ also shows obvious differences compared with those under the other two Ca, i.e. the neck region is shorter and the final collapse generates a much larger satellite droplet at the neck centre. The effects of inertia are thus expected to play a major role in the breakup dynamics under $Ca = 2.0 \times 10^{-3}$. Since we focus on the breakup dominated by capillary, conditions under Ca on the order of 10^{-4} or smaller are considered to eliminate the effects of inertia.

The neck evolutions during the axisymmetric breakup of the confined fluid thread are characterized by two principal radii at the neck centre, R_1 and R_2, in the radial and axial directions (figure 1a), respectively, and the mean radius R_m is $R_1R_2/(R_1 + R_2)$ according to the Young–Laplace equation. Figures 3(a) and 3(b) show the evolutions of R_1 and R_m for $Ca = 2.0 \times 10^{-4}$ and 2.0×10^{-5}, respectively, where $\tau = t_c - t$ represents the time remaining until pinch-off, with t the time and t_c the time at pinch-off. The radii are normalized by R, and time is scaled by R/U. Note that, the normal direction of the neck surface is chosen here to point from the surface to the inside of the fluid thread. R_1 is always positive since the centre of R_1 is on the same side as the surface normal, while R_2 is negative when the centre of R_2 is on the opposite side of the surface normal, as it is during most of the time of the breakup. The centre of R_2 moves to the positive side of the surface normal, as it is at the final moments of the breakup due to the formation of the satellite droplet at the centre. In figure 3(a,b), we identify two stages where R_1 and R_m exhibit power law behaviours with τ^α, where the scaling constant α is a signature of the physical mechanisms causing the collapse (van Hoeve *et al.* 2011). In the earlier necking stage before the first collapse stage for both Ca numbers, the variations in the radii do not conform to any power law with

https://doi.org/10.1017/jfm.2019.426 Published online by Cambridge University Press

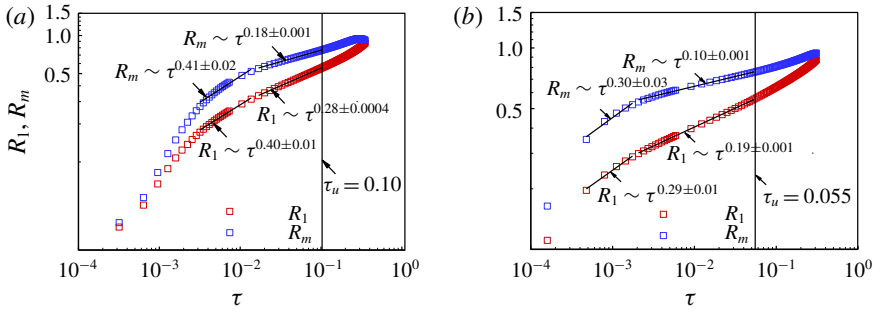


FIGURE 3. (Colour online) Time evolutions of R_1 and R_m for axisymmetric breakup of a confined fluid thread under Ca of 2.0×10^{-4} (a) and 2.0×10^{-5} (b).

a constant α. We thus expect a critical condition representing the transition between the earlier necking stage and the collapse stages.

From the evolution of the flow field, we find a transition of the flow pattern near the neck. As shown in figure 4(a), oil flows expansively to squeeze the interface at $t = 0.41$ and 0.45, while oil flows towards the neck centre at t = 0.48 and 0.51. We obtain the critical time t_u representing the flow transition with the help of the stop-flow method (Stone, Bentley & Leal 1986; Blanchette & Bigioni 2006; Hoang *et al.* 2013). For a given simulation, resumable files are saved at different moments. For each file, the flow is stopped by setting the velocities of both the flow field and the inlet to zero. The resumable files are then carried on to determine t_u by distinguishing different flow patterns. For $Ca = 2.0 \times 10^{-5}$, we obtain t_u and the corresponding critical mean radius R_m^u, (0.76 ± 0.002). If the flow stops when $R_m > R_m^u$, as shown in figure 4(b), the interface remains stationary after small relaxations (at $t = 0.4459$ and 0.4745). If the flow stops when $R_m < R_m^u$, the neck thins spontaneously until it collapses (at $t = 0.4777$). The mean radius of the stationary interface, corresponding to R_m^u, R_m^{st}, is approximately 0.72. The critical remaining time $\tau_u = t_c - t_u$ is obtained for each Ca number, as in figure 3(a,b). Here τ_u preferably represents the duration of the late collapse stage, indicating that the transition of the flow pattern is equivalent to the transition between the earlier necking stage and the later collapse stage.

The existence of the abovementioned transition is further confirmed by stop-flow experiments in a flow-focusing microfluidic device with circular channels fabricated by the rapid prototyping method. As shown in figure 4(c), water flows into the channel junction from the left inlet and oil flows into the junction from the top and bottom inlets. Note that, since the flow rate of the oil phase is low, the interface is expected to have a rapid response to the oil flow to make the neck region axisymmetric. The physical and geometrical parameters are $\mu_w = 1$ mPa s, $\rho_w = 998$ kg m^{-3}, $\mu_o = 20$ mPa s, $\rho_o = 950$ kg m^{-3}, $\sigma = 35$ mN m^{-1}, and $R = 400$ μm. During the stop-flow experiments, the water flow is switched off after the thread tip passes the channel junction. The oil flow is intermittently stopped and resumed to determine the critical shape of the neck. A MATLAB code (provided in the supplementary material) has been written to measure the two principal radii at the neck centre, as indicated in figure 4(c). The critical mean radius, R_m^u, is found to be (0.79 ± 0.04), in agreement with the value of (0.76 ± 0.002) obtained from simulations. When the flow stops at $R_m > R_m^u$, the interface relaxes inwards, as in the simulations, and then slowly moves outwards. This outward motion may be attributed to the leakage of oil from the neck

https://doi.org/10.1017/jfm.2019.426 Published online by Cambridge University Press

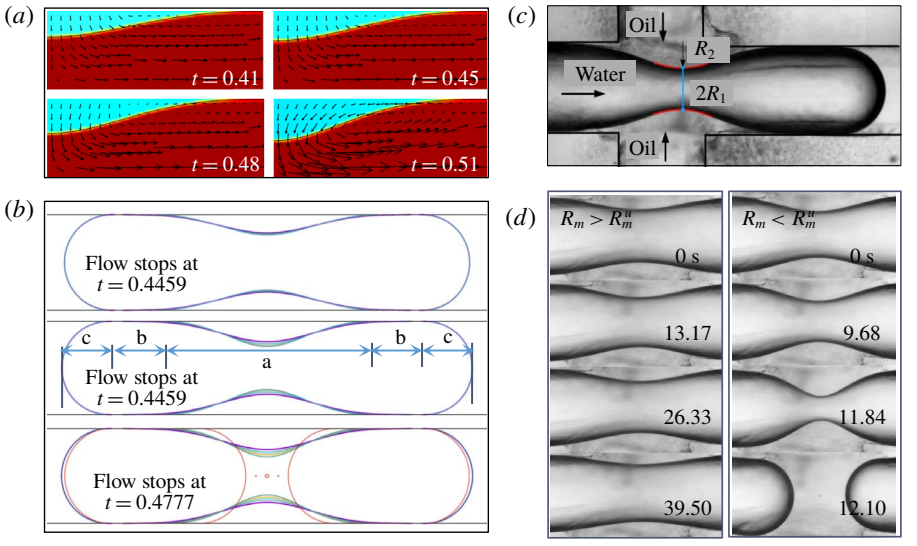


FIGURE 4. (Colour online) Determination of the critical mean radius R_m^u at the neck centre for axisymmetric configurations. (*a*) Transition of the flow pattern during breakup for $Ca = 2.0 \times 10^{-5}$. (*b*) Evolution of the interface during stop-flow simulations. The initial shapes are adapted from the simulation for $Ca = 2.0 \times 10^{-5}$. (*c*) Stop-flow experiments to determine R_m^u. Supplementary movies 1 and 2 are for $R_m > R_m^u$ and $R_m < R_m^u$, respectively.

region through the gaps between the rough channel wall and the interface. When the flow stops at $R_m < R_m^u$, the neck collapses irreversibly, as in the simulations.

3.2. *Destabilizing mechanism of axisymmetric fluid threads*

The above stop-flow studies provide direct evidence that the earlier necking stage is quasi-stable (Garstecki *et al.* 2005). Our simulations suggest that the internal pressure of the droplet is nearly constant during the quasi-stable necking stage. Using the pressure outside of the droplet tips as the reference pressure, the internal pressure of the fluid thread can be estimated by the capillary pressure of the tips, σ/R_m, which equals $2\sigma/R$ since $R_m = R/2$ ($R_1 = R_2 = R$ at the tips). Additionally, the oil pressure outside the neck is almost evenly distributed during the quasi-stable stage. The capillary pressure is thus nearly constant along the neck interface, indicating that R_m can be considered constant along the neck region. In the axisymmetric configuration, the neck interface is essentially a surface of revolution with constant mean curvature or a Delaunay surface (Delaunay 1841). R_m varies from R to approximately $0.76R$ in the quasi-stable stage. The corresponding capillary pressure, varying from σ/R to $1.32\sigma/R$, is consistently smaller than the internal pressure, $2\sigma/R$. The internal pressure pushes the interface outwards to stabilize it against inward collapse. The stabilization of the confined fluid thread thus originates from the domination of the internal pressure caused by the thread tips under confinement.

The constant-mean-curvature feature of the neck interface inspires us to propose a theoretical analysis to reveal an unrecognised destabilizing scenario of the capillary instability. As shown in figure 4(*b*), the shape of a tightly confined droplet can be divided into three types of regions at low flow-rate conditions: (a) the neck region, (b) two cylindrical regions and (c) two hemispherical head-ends. If representing the

https://doi.org/10.1017/jfm.2019.426 Published online by Cambridge University Press

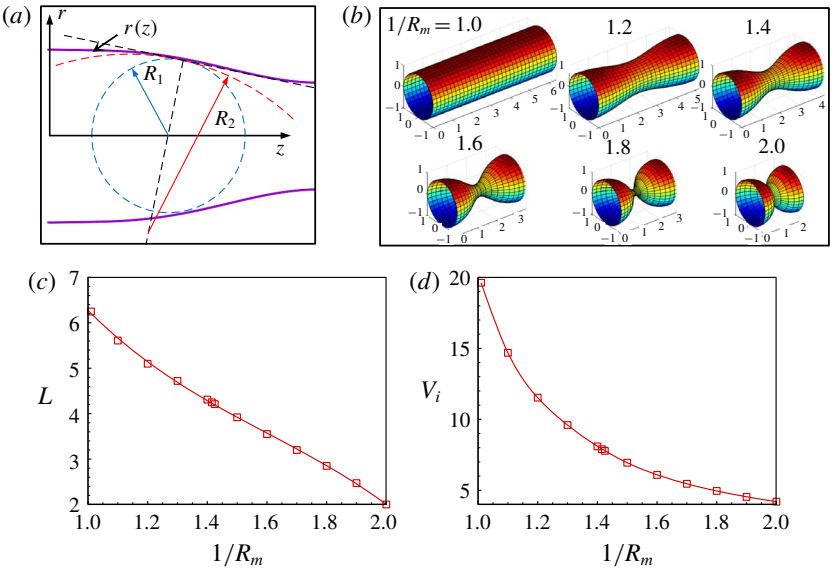


FIGURE 5. (Colour online) (*a*) Sketch of the neck profile consisting of a constant-mean-curvature curve. (*b*) Axisymmetric constant-mean-curvature surface with increasing $1/R_m$. (*c*) Variation of the length of the neck region with $1/R_m$. (*d*) Variation of the volume contained by the constant-mean-curvature surface with $1/R_m$.

neck profile as $r(z)$ in the rotating coordinate system shown in figure 5(*a*), the two principal radii of curvature are derived from geometrical relationships as

$$R_1(z) = r(z)[1 + \dot{r}(z)^2]^{1/2} \tag{3.1}$$

and

$$R_2(z) = -\frac{[1 + \dot{r}(z)^2]^{3/2}}{\ddot{r}(z)}, \tag{3.2}$$

respectively. We consider a general situation in which the fluid thread is long enough to have all three types of regions during the breakup. Boundary conditions of $r(0) = R$ and $\dot{r}(0) = 0$ are thus valid at the junction between the neck and cylindrical regions. The shapes of the neck for $1/R \leqslant 1/R_m \leqslant 2/R$ are obtained by solving

$$1/R_m = 1/R_1(z) + 1/R_2(z) \tag{3.3}$$

using a MATLAB code (provided in the supplementary material). Note that it is possible to predict the shape of the entire fluid thread since the only additional variable for a given $1/R_m$ is the length of each cylindrical region, which can be obtained from volume conservation. Figure 5(*b*) shows the shapes of the constant-mean-curvature surface with the variation of $1/R_m$. The shape changes from cylindrical to two intersecting hemispheres. The length of the neck region L decreases near-linearly with $1/R_m$, as shown in figure 5(*c*). The initial cylindrical shape has a maximum length of $2\pi R$, according to Delaunay (1841). The length decreases to $2R$ for $1/R_m = 2R$. The volume contained by the constant-mean-curvature surface V_i also decreases with $1/R_m$, as shown in figure 5(*d*) (scaled by R^3).

https://doi.org/10.1017/jfm.2019.426 Published online by Cambridge University Press

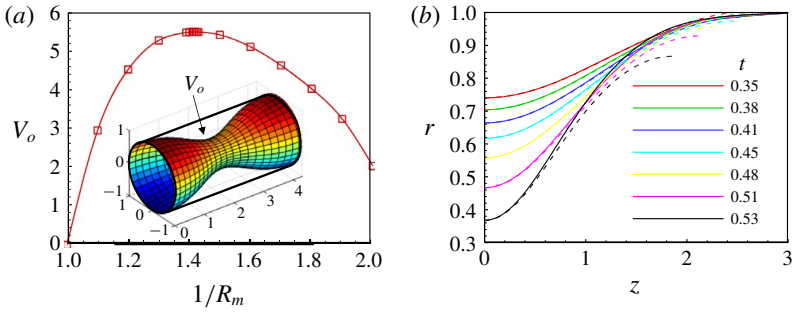


FIGURE 6. (Colour online) (*a*) Evolution of the oil volume between the interface and the cylindrical channel with the mean curvature for the constant-mean-curvature surface. (*b*) Comparison of the neck profiles between the numerical simulations (solid lines) and constant-mean-curvature profiles (dashed lines) using the neck radii from the simulations as boundary conditions.

It is interesting to note that the volume between the neck interface and the columnar channel wall V_o increases first and then decreases with increasing $1/R_m$ as shown in figure 6(*a*). During the whole process of necking, oil inevitably flows into the channel, resulting in the oil volume increasing with $1/R_m$ during the breakup. When the volume is larger than the maximum allowed for the constant-mean-curvature surfaces, R_m can no longer be constant along the neck interface. A capillary pressure gradient thus emerges along the interface to promote an irreversible collapse. Figure 6(*a*) shows that the maximum oil volume for the constant-mean-curvature surfaces occurs at $R_m = (0.71 \pm 0.001)$. The corresponding V_o is approximately 5.45. This critical R_m is in good agreement with R_m^{st} obtained numerically for $Ca = 2.0 \times 10^{-5}$, approximately 0.72. We support this finding directly by comparing the simulated neck profiles for $Ca = 2.0 \times 10^{-5}$ with the corresponding constant-mean-curvature profiles as shown in figure 6(*b*). The constant-mean-curvature profiles are calculated by solving (3.3) using the values of R_1 and R_m at the neck centre as boundary conditions. Good agreements are achieved before the critical moment t_u, approximately 0.48. Note that there are disparities between the numerical and theoretical profiles near the joint of the neck region and the cylindrical region. They are likely due to dynamical effects in the flow-field that increase the oil pressure near the joint. Obvious differences are observed after t_u, indicating that the neck profiles are no longer constant-mean-curvature profiles. The destabilization of the axisymmetrically confined fluid threads is clearly the result of the gradient of the capillary pressure induced by the confinements of both geometry and flow. This instability scenario can be termed confinement-induced capillary instability.

To further validate the above finding, we calculate the static shapes of an axisymmetrically confined fluid thread for given V_o (scaled by R^3) using the Surface Evolver program that is able to evolve the surface towards its minimal energy (Brakke 1992). A fluid thread with a fixed volume is constrained in a circular tube. The outer fluid with a volume of V_o is placed at the centre of the fluid thread to encircle it. Figure 7(*a*) shows several static shapes under different V_o. The fluid thread is stable as V_o varies from 0 to 5.46. When $V_o = 5.47$, the fluid thread becomes unstable and the interfacical meshes collapse to the centre since the Surface Evolver program cannot handle a topological change of interface. The critical V_o is in good agreement with the above theoretical prediction, i.e. approximately 5.45. As shown

https://doi.org/10.1017/jfm.2019.426 Published online by Cambridge University Press

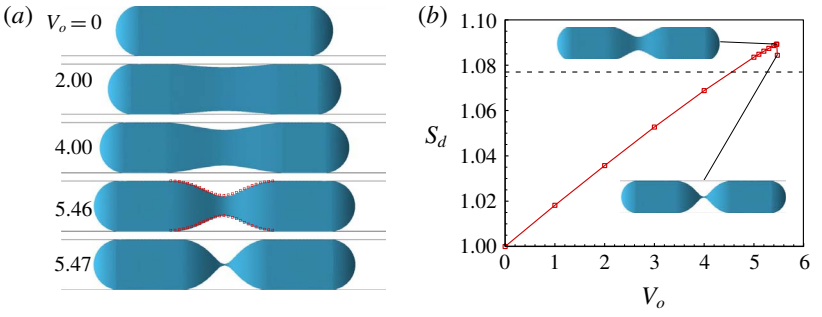


FIGURE 7. (Colour online) (*a*) Static shapes of axisymmetrically confined fluid thread obtained by Surface Evolver for given V_o. (*b*) Variation of the interfacial energy of the confined fluid thread S_d with V_o.

in figure 7(*a*), the critical neck profile predicted theoretically is overlapped onto the static shape for $V_o = 5.46$, further indicating the good agreement. Figure 7(*b*) shows that the interfacial energy of the fluid thread S_d increases with V_o until $V_o = 5.46$. When $V_o = 5.47$, the interfacial energy is released to show a sudden jump. Note that, in practice, the fluid thread breaks into two identical droplets with round ends at $V_o = 5.47$. The corresponding S_d can be calculated from volume conservation, as indicated by the dashed line in figure 7(*b*). The energy plot indicates that there is an energy barrier, determined by the critical shape, that must be overcome to induce the capillary instability.

Additional simulations are carried out to investigate the influences of Ca and the physical parameters of the two fluids on the critical neck shape. For the first case, only U is altered to be 1/10 of that in the case in figure 3(*b*), with a corresponding Ca of 2.0×10^{-6}. The top and bottom images in figure 8(*a*) show the evolutions of the interface when the flow is stopped just before and after the critical moments, respectively. We find R_m^u is measured to be approximately $0.73R$ and R_m^{st} is approximately $0.71R$, which is very close to the theoretical prediction. This means that R_m^u and R_m^{st} obtained from the stop-flow simulations converge to the theoretical value of $0.71R$ as Ca decreases and approaches 0. For the second case, water is changed to air based on the case in figure 3(*b*). R_m^u obtained from the stop-flow simulations in figure 8(*b*) is approximately $0.76R$ and R_m^{st} is approximately $0.71R$. For the third case, the viscosity ratio of the oil and water is reduced from 8 to 4, while the interfacial tension is increased from 5 mN m^{-1} to 10 mN m^{-1}. The corresponding capillary number Ca is 1.0×10^{-5}. Stop-flow simulations in figure 8(*c*) indicate that R_m^u and R_m^{st} are approximately $0.75R$ and $0.72R$, respectively. For the fourth case, we further reduce the viscosity ratio from 4 to 1 and increase the interfacial tension from 10 mN m^{-1} to 40 mN m^{-1}. The corresponding Ca is 2.5×10^{-6}. R_m^u and R_m^{st} are then $0.72R$ and $0.71R$, respectively. The critical neck profile predicted theoretically is overlapped onto the top images in the four frames in figure 8, to show the agreements between the numerical simulations and the theoretical prediction. Therefore, it is safe to conclude that the confinement-induced capillary instability is not affected by the physical parameters of the two fluids.

Droplet-based microfluidics utilizes the breakup of a confined fluid thread to generate monodispersed droplets. Microfluidic channels fabricated by soft lithography have rectangular cross-sections. To determine if the confinement-induced mechanism

https://doi.org/10.1017/jfm.2019.426 Published online by Cambridge University Press

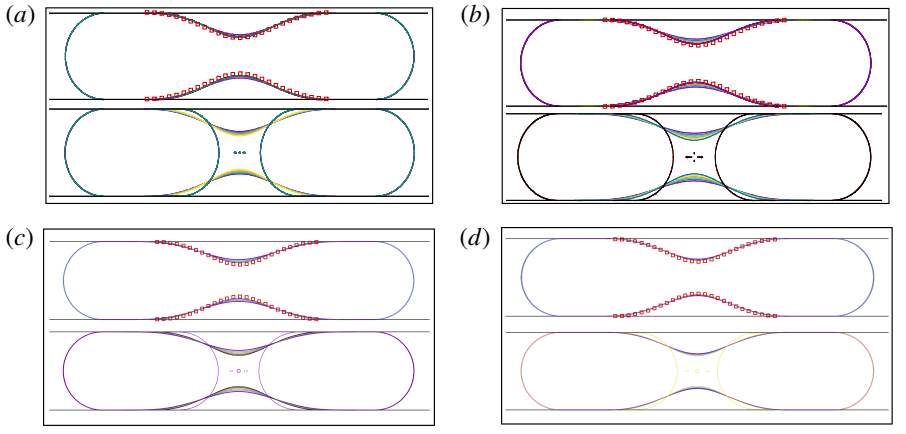


FIGURE 8. (Colour online) Interfacial evolutions just before and after the critical moments determined by stop-flow simulations for four conditions with different flow and physical parameters. The top and bottom images in each of the four frames are for before and after the critical moments, respectively. (*a*) Only U is altered to be $1/10$ of that in the case in figure 3(*b*). The corresponding capillary number Ca is 2.0×10^{-6}. (*b*) Water is changed to air based on the case in figure 3(*b*). (*c*) The viscosity ratio of oil and water is 4, while the interfacial tension is 10 mN m^{-1}. The corresponding Ca is 1.0×10^{-5}. (*d*) The viscosity ratio of oil and water is 1, while the interfacial tension is 40 mN m^{-1}. The corresponding Ca is 2.5×10^{-6}.

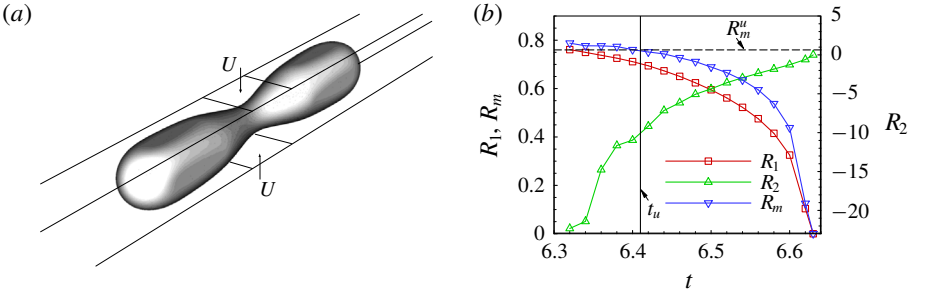


FIGURE 9. (Colour online) Droplet breakup in a flow-focusing configuration with a square microchannel. (*a*) Schematic of the simulation set-up. (*b*) Time evolutions of the three radii for $Ca = 6.2 \times 10^{-4}$. The three radii are scaled with $H/2$, and the time is scaled with $H/2U$. The critical time t_u is determined by stop-flow simulations.

is valid for fluid threads in rectangular channels, droplet breakup in a flow-focusing configuration with a square microchannel is studied numerically. As shown in figure 9(*a*), the oil phase with a velocity of U flows into the channel with a height H (25 μm) and from the top and bottom openings to squeeze a long water droplet at its centre. The physical parameters are the same as those in figure 3. The time evolutions of the three radii for $Ca = 6.2 \times 10^{-4}$ are shown in figure 9(*b*). We find that the neck region is approximately axisymmetric at the centre since Ca is small. Stop-flow simulations demonstrate that $R_m^u = (0.76 \pm 0.01)(H/2)$, agreeing with that in the axisymmetric configuration. The confinement-induced capillary instability is

https://doi.org/10.1017/jfm.2019.426 Published online by Cambridge University Press

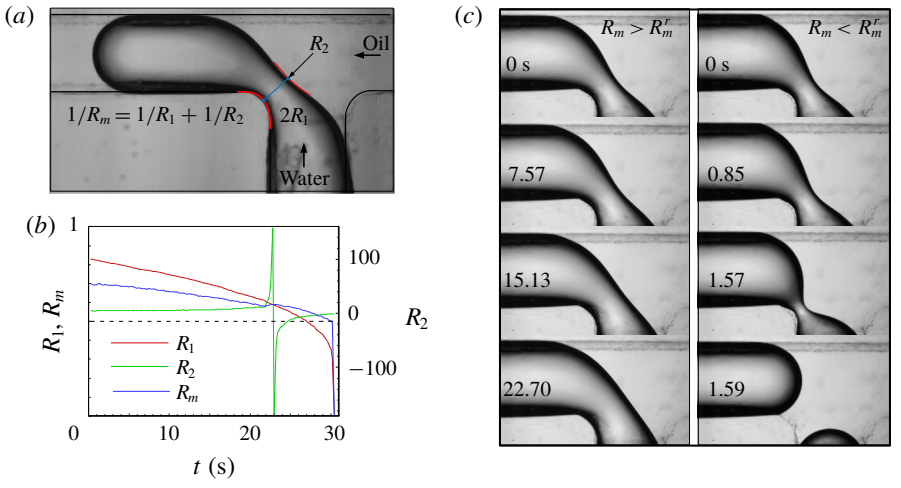


FIGURE 10. (Colour online) Rapid collapse of the neck region and determination of the critical mean radius at the neck centre R_m^r. (*a*) Experimental configuration and measurements of two principal radii of curvature for fluid thread breakup in a T-junction of a cross-flowing configuration. The physical parameters are the same as those in figure 2(*c*). (*b*) Time evolution of the radii at the neck centre for $Ca = 2.0 \times 10^{-5}$. (*c*) Interfacial evolution before and after the critical moment from experiments using the stop-flow method. Supplementary movies 3 and 4 are for $R_m > R_m^r$ and $R_m < R_m^r$, respectively.

thus also applicable for fluid threads in square microchannels, as long as the fluid thread has an axisymmetric neck region.

3.3. *Destabilizing mechanism of non-axisymmetric fluid threads*

The above investigations combine simulations, experiments, and theory to reveal the confinement-induced breakup mechanism of axisymmetric fluid threads. We also experimentally study the breakup of a non-axisymmetric fluid thread with circular channels in a cross-flowing configuration, as shown in figure 10(*a*). The channel diameter and the fluid properties are the same as those in figure 4(*c*). Water and oil flow from the bottom and right inlets, respectively, into the channel junction. The water thread is squeezed by the oil phase to break up at the channel junction into water droplets. The usage of circular channels avoids leakage in the corners of rectangular channels. This enables us to investigate the fluid thread breakup in the cross-flowing configuration under an extremely low flow-rate condition. It is thus reasonable to assume that the main radius is constant around the cross-section of the neck centre, except the region that contacts with the wall. The shape of the neck can then be represented by the two principal radii indicated in figure 10(*a*). Figure 10(*b*) shows the evolution of the three radii measured from high-speed images under $Ca = 2.0 \times 10^{-5}$. The measurement procedure and code can be found in the supplementary material. The collapse occurs more rapidly than that in the axisymmetric configuration, suggesting the existence of a different destabilization mechanism. The stop-flow experiment in figure 10(*c*) shows that the critical mean radius R_m^r is $(0.51 \pm 0.01)R$. The capillary pressure at the neck centre is approximately $2\sigma/R$, which is equal to the internal pressure of the fluid thread determined by the

https://doi.org/10.1017/jfm.2019.426 Published online by Cambridge University Press

hemispherical tip with R_m of $R/2$, i.e. $0.50R$. The destabilizing mechanism is thus quite simple – the fluid thread becomes unstable when the capillary pressure at the neck centre balances the internal pressure.

Several destabilizing mechanisms, essentially the same as the one described above, have been identified in other confined situations. For example, approximately half a century ago, Roof (1970) considered the breakup of an oil thread inside a water-filled pore. He indicated theoretically, based on the balancing of the capillary pressure, that for a given shape of constriction, there is a minimum size to the protruding portion of the oil that permits breakup. Subsequently, Beresnev, Li & Vigil (2009) analysed the distribution of the capillary pressure in a channel with a sinusoidal profile. A geometrical criterion for the spontaneous breakup was developed by comparing the capillary pressure in the troughs to that in the crests. The criterion reduces to the condition for the occurrence of the R–P instability for a free liquid jet in gas. For a fluid thread in a step-emulsification microfluidic device with rectangular channels, a so-called 'curvature balance model' for droplet breakup was proposed based on a quasi-static balance between the curvature of the thread inside the inlet channel and the curvature of the 'bulb' downstream of the step (Dangla *et al.* 2013). It was also found that the balance is not dependent upon the fluid properties.

The breakup of a fluid thread in a cross-flowing configuration with rectangular microchannels was believed to be triggered by the backward flow in the corners, from the thread tip to the neck (van Steijn *et al.* 2009). They used the pressure in the gas thread as the reference pressure to calculate the pressure in the liquid at the squeezing interface and at the thread tip. The pressure difference over the gutters was thus expressed by subtracting the latter pressure from the prior pressure. Experimental measurements of the radii showed that the pressure difference changes sign when the gas thread begins to collapse. This proposed critical condition was indeed essentially the same as the abovementioned mechanism based on the balancing of the capillary pressure. However, it was believed that this change causes the reversed flow in the gutters, which drives the liquid back to the squeezed neck to force the thread to collapse. The existence of the backward flow was determined through the observation of velocity fields only near the neck region (van Steijn *et al.* 2009). Conversely, our experiments involving a cross-flowing configuration with a circular cross-section (figure 10) demonstrate that the critical geometrical condition happens even when there is no corner at all. To look into this contradiction, numerical simulations are carried out for a fluid thread in a cross-flowing configuration within square microchannels. The channel height and fluid properties are the same as those in the simulations in figure 9. The velocity vectors in the plane of $0.1H$ from the top wall are shown in figure 11 for two situations with different lengths of the generated droplets. It is clear that the backward flow in the corners does not start from the thread tip, but only exists near the neck region. The accelerating collapse of the neck region causes the backward flow that drives the oil phase towards the neck centre, similar to the axisymmetric breakup in figure 4(*a*).

For another non-axisymmetric configuration, droplet breakup in a T-junction (as shown in figure 12*a*), Hoang *et al.* (2013) stated that the autonomous breakup starts when the curvature at the neck becomes larger than the curvature everywhere else. The mechanism responsible for the autonomous breakup was believed to be similar to the end-pinching mechanism (Stone *et al.* 1986). However, the end-pinching mechanism was proposed analytically to be a consequence of the motion generated via capillary pressure gradients in the region near the end of the droplet (Stone *et al.* 1986), not via the competition of the curvatures that determines the capillary

https://doi.org/10.1017/jfm.2019.426 Published online by Cambridge University Press

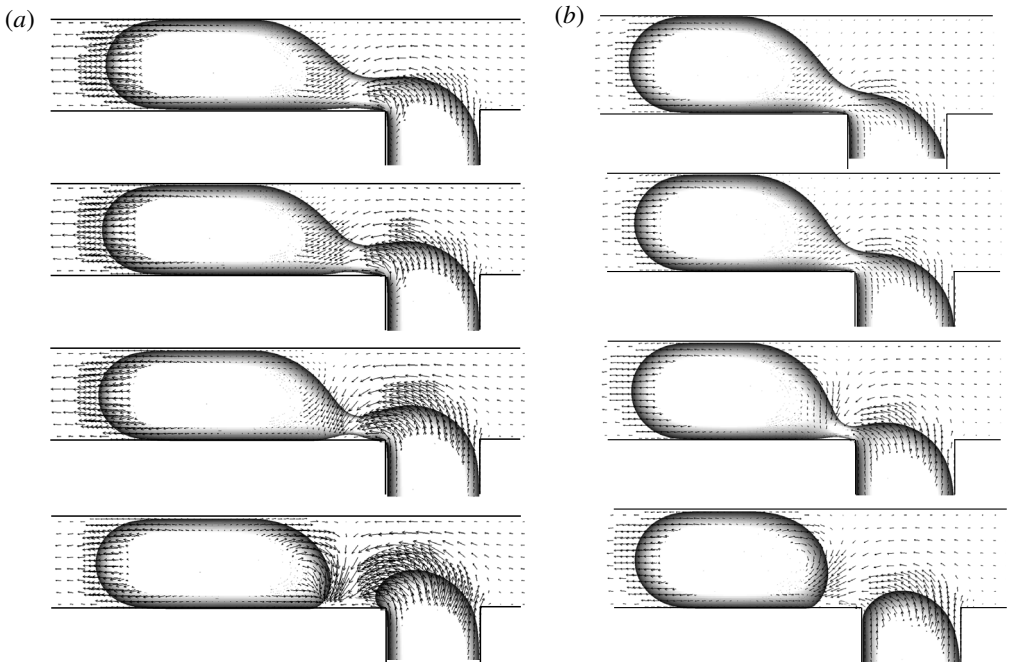


FIGURE 11. Velocity vectors in the plane of $0.1H$ from the top wall during the thread breakup in a T-junction. The capillary number based on the oil phase is 6.2×10^{-4}. The lengths of the generated droplets are approximately $2.5H$ (a) and $2.0H$ (b) by varying the flow rate of the water phase.

pressure. Meanwhile, Hoang *et al.* (2013) obtained a simple relation between the critical neck thickness (twice the R_1 defined here) for autonomous breakup and the height-to-width ratios of the rectangular channels. Since the relation was the same as that for the cross-flowing configuration, Hoang *et al.* (2013) suggested that the breakup mechanism was similar to the aforementioned backward-flow mechanism (van Steijn *et al.* 2009). The breakup mechanism of droplet breakup in a T-junction is thus still unclear. The accuracy is also questionable when using R_1 to represent the neck shape.

We revisit droplet breakup in a T-junction through numerical simulations. The geometrical set-up is shown in figure 12(a), where a T-junction comprises two square microchannels. The oil phase flows with a velocity U into the T-junction from one channel to deform a confined water droplet at the centre of the T-junction. The fluid properties are the same as those for the axisymmetric simulations in § 3.1 and H of the square channels is 30 μm. Both the fluid properties and geometrical parameters are identical to those in previous experimental (Link *et al.* 2004; Jullien *et al.* 2009) and numerical (Hoang *et al.* 2013) studies. Figure 12(b) depicts the evolutions of R_1 and the three mean radii at three key positions of the neck centre under $Ca = 6.2 \times 10^{-4}$. As indicated in figure 12(c), the three mean radii are the top and bottom mean radii from the top view, R_m^t and R_m^b, and the mean radius from the side view, R_m^s. Owing to the asymmetric flow, the three radii are not equal. R_m^t is larger than R_m^b since the oil flow compresses the droplet from the top. Figure 13(a) shows the evolutions of the droplet profiles on the longitudinal symmetry plane and the cross-section across the neck centre. As the profiles have the same time interval,

https://doi.org/10.1017/jfm.2019.426 Published online by Cambridge University Press

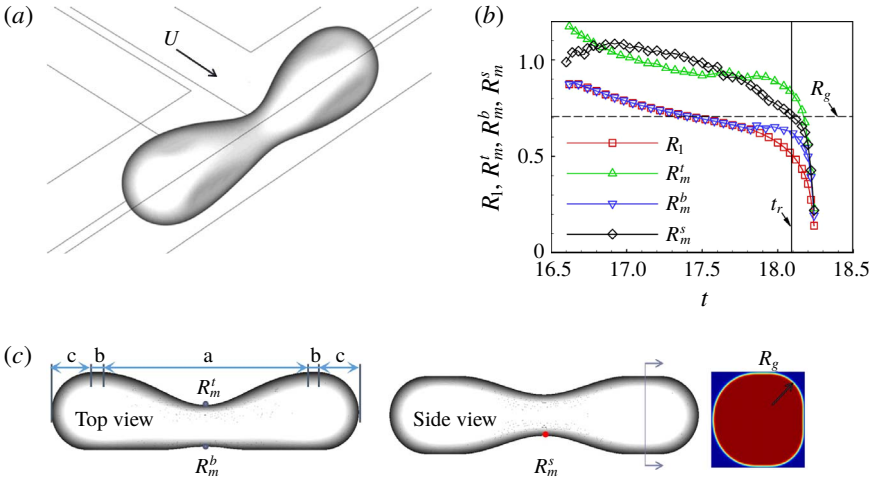


FIGURE 12. (Colour online) Droplet breakup in a T-junction. (*a*) The schematic diagram of the simulation set-up. (*b*) The time evolution of the radii for $Ca = 6.2 \times 10^{-4}$. (*c*) The critical droplet shape determined by stop-flow methods.

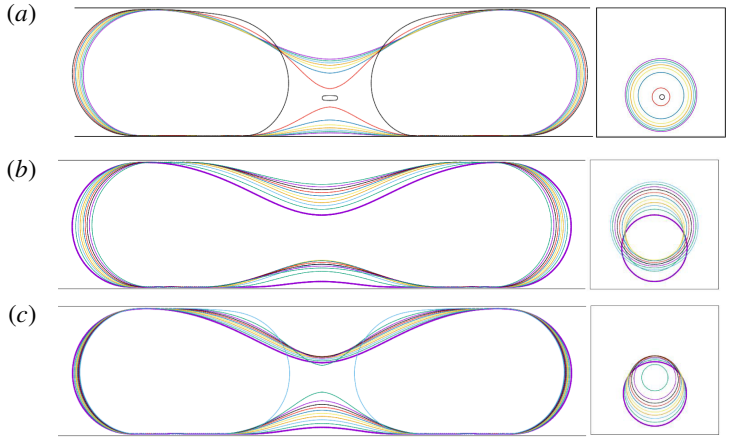


FIGURE 13. (Colour online) Evolutions of droplet profiles on the longitudinal symmetry plane and the cross-section across the neck centre, during the breakup under $Ca = 6.2 \times 10^{-4}$, when flow stops just before (*b*) and after (*c*) the critical moment.

a rapid change of the neck profile is observed close to the final breakup. The profiles of the cross-section are circles which are nearly concentric.

Stop-flow simulations are carried out to obtain the critical neck shape as shown in figure 12(*c*). R_1 at the critical moment t_r is found to be approximately $0.52(H/2)$, agreeing with $0.53(H/2)$ in Hoang *et al.* (2013). Non-negligible distinctions between R_1 and the three mean radii at t_r are observed in figure 12(*b*), indicating that it is not accurate to use σ/R_1 to represent the capillary pressure. The evolutions of the droplet profiles when the flow is stopped just before and after t_r are shown in figures 13(*b*) and 13(*c*), respectively. When the flow is stopped just before t_r, the neck centre moves towards the oil inlet. After the neck centre reaches the centre of the channel, the

https://doi.org/10.1017/jfm.2019.426 Published online by Cambridge University Press

neck shape becomes nearly axisymmetric and expands slowly owing to the leakage of the oil phase from the corners. When the flow is stopped just after t_r, the motion of the interface at the neck centre couples both the motion towards the oil inlet and the collapse motion towards the neck centre. The profiles on the cross-section show a consistent decrease of R_1. The upper profile on the longitudinal symmetry plane moves towards the oil inlet first and then collapses towards the neck centre. The motion towards the oil inlet indicates that, after the oil flow is stopped, the internal pressure inside the neck turns to push the upper interface outward to stabilize the interface. Naturally, the shape of the upper interface cannot be expected to represent the critical neck shape.

The abovementioned breakup mechanism for a fluid thread in the cross-flowing configuration inspires us to look into the internal pressure of a droplet in a rectangular channel. For a static non-wettable long fluid thread in a rectangular channel, the internal pressure of the droplet is σ/R_m^{un}, where R_m^{un} is the mean radius of the unconfined droplet interface, including the droplet tips and corner interface at the columnar region (Wong, Radke & Morris 1995). R_m^{un} at the corner interface reduces to the radius of the circular arcs R_g in the cross-section of the columnar region. Utilizing this geometrical feature, Wong *et al.* (1995) developed an explicit solution of R_g for a static non-wettable long fluid thread under $Ca \to 0$, i.e.

$$R_g^{st} = \lambda H/[1 + \lambda + [(1-\lambda)^2 + \pi\lambda]^{1/2}], \tag{3.4}$$

where λ is the ratio of the channel width W and height H. For the square channel here, $\lambda = 1$ and $R_g^{st} \approx 0.53(H/2)$. Under a finite Ca, the interface is altered by the droplet motion and the corner flow around the droplet to divide the mean radius from R_g^{st} (Wong *et al.* 1995). We then quantify the internal pressure by measuring R_g from the cross-section of the columnar region in figure 12(*c*). Due to the asymmetry of the flow-field, R_g at the left two corners are larger than those at the right two corners. The smaller R_g at the right corners thus determines the internal pressure through a higher capillary pressure. Here R_g stays constant during the breakup and is measured to be approximately $0.71(H/2)$. When R_g is indicated on figure 12(*b*) with a dashed line, we find that it is approximately equal to R_m^s at t_r, $(0.70 \pm 0.02)(H/2)$. The equality relation of the critical R_m^s and R_g indicates essentially the same breakup mechanism as for the abovementioned fluid threads in a cross-flowing condition. Again, the fluid thread becomes unstable when the capillary pressure at the neck centre balances the internal pressure, which occurs here, only at parts of the neck interface due to the asymmetric flow under a finite Ca.

3.4. *Critical droplet lengths for obstructed breakup*

The above analyses show that the critical conditions for the onset of capillary instability for small Ca numbers are geometrical for confined fluid threads. This finding is consistent with previous experimental studies (Link *et al.* 2004; Jullien *et al.* 2009) on droplet breakup in a T-junction. Jullien *et al.* (2009) classified the droplet dynamics into non-breakup, non-obstructed breakup, and obstructed (or blocked) breakup. For obstructed breakup, the droplet touches the walls of the T-junction, i.e. droplets keep obstructing the T-junction before breakup. For non-breakup and non-obstructed breakup, there is a tunnel between the droplet and the wall. A droplet shorter than a Ca-dependent length opens a tunnel on one side of the junction by a random disturbance, and eventually moves in the opposite direction without breakup.

https://doi.org/10.1017/jfm.2019.426 Published online by Cambridge University Press

A longer droplet can break under the non-obstructed condition. When Ca is low enough, the non-obstructed breakup cannot happen. Jullien *et al.* (2009) identified experimentally that there exists a critical initial droplet length, L_{cr}. For a droplet with a length larger than L_{cr}, obstructed breakup happens, independent of Ca. Inspired by this finding, we predict L_{cr} based on the critical neck shape from the stop-flow simulations as shown in figure 12(c). The critical droplet shape from the top view in figure 12(c) can be divided into five regions: the neck region (a), two plug-shaped regions (b) and two hemispherical head-ends (c). For different initial droplet lengths, neither the critical shape of the neck region nor the shape of the head-ends changes. The shortest breakable droplet should thus have a volume that comprises only those of the neck region and two head-ends. A shorter droplet cannot reach the critical neck shape for obstructed breakup since the volume is not large enough to reach the critical neck shape for breakup. According to the critical droplet shape in figure 12(c), L_{cr} is calculated by subtracting the length of the two plug-shaped regions from the length of the initial droplet to give approximately $3.07H$. This length is close to πH, which is used by Link *et al.* (2004) to predict the boundary between no breakup and breakup according to the R–P stability criterion for the same combination of fluids. Jullien *et al.* (2009) found that L_{cr} is altered by the viscosity ratio of the dispersed and continuous phases, and is $2.62H$ and $4.20H$ for a viscosity ratio of 0.11 and 1.67, respectively. For the fluids considered here, the viscosity ratio is approximately 0.13. The L_{cr} obtained is thus consistent with the experimental study of Jullien *et al.* (2009). It is likely that the viscosity ratio influences the critical shape through the asymmetric flow field around the neck and the leakage flow at the corners.

Similarly, L_{cr} for the axisymmetric configuration in figure 1(a) can be determined theoretically (corresponding to the critical $R_m = 0.71R$) to be approximately $4.52R$ or $2.26D$ (with the diameter $D = 2R$). Simulations with different initial droplet lengths are carried out for $Ca = 2.0 \times 10^{-4}$, 2.0×10^{-5} and 2.0×10^{-6} to find L_{cr} for the obstructed breakup. Different from the simulations in figure 1, that consider the obstructed breakup using only a quarter of the cross-section of the configuration, half of the cross-section is used here to consider the situations of non-breakup and non-obstructed breakup (see the supplementary material for the schematic of the computational domain). All three types of droplet dynamics are obtained for $Ca = 2.0 \times 10^{-4}$, but only non-breakup and obstructed breakup are observed for Ca of 2.0×10^{-5} and 2.0×10^{-6}. Figure 14(a) shows the droplet dynamics for $Ca = 2.0 \times 10^{-4}$ under different initial droplet length L. When $L = 1.75D$, the neck region cannot reach the critical shape for breakup. The droplet moves to one side due to the asymmetric flow outside the neck surface. When $L = 2.00D$, the droplet breaks with a tunnel between the interface and the wall. When the tunnel vanishes, the neck evolutions are obviously the same for $L = 2.45D$, $3.00D$ and $4.00D$. Previous experiments (Jullien *et al.* 2009) distinguished non-obstructed breakup and obstructed breakup by the width of the opening tunnel. If the width was below the optical resolution, the breakup was classified as the obstructed one. Our work is different in that we use the time period required for breakup t_b to distinguish these two types of breakup. Figure 14(b) shows that t_b decreases with L but then shows independence of L. The physical reason for the independence is that, when the droplet length is large enough to cause obstructed breakup, the shape revolution at the neck region will not be affected by L. L_{cr} for $Ca = 2.0 \times 10^{-4}$ is thus obtained from figure 14(b) to be approximately $2.43D$. This value is in agreement with the theoretical prediction of $2.26D$. The difference between the theoretical and numerical predictions may be due to the disparities between the numerical and theoretical neck profiles near the joint

https://doi.org/10.1017/jfm.2019.426 Published online by Cambridge University Press

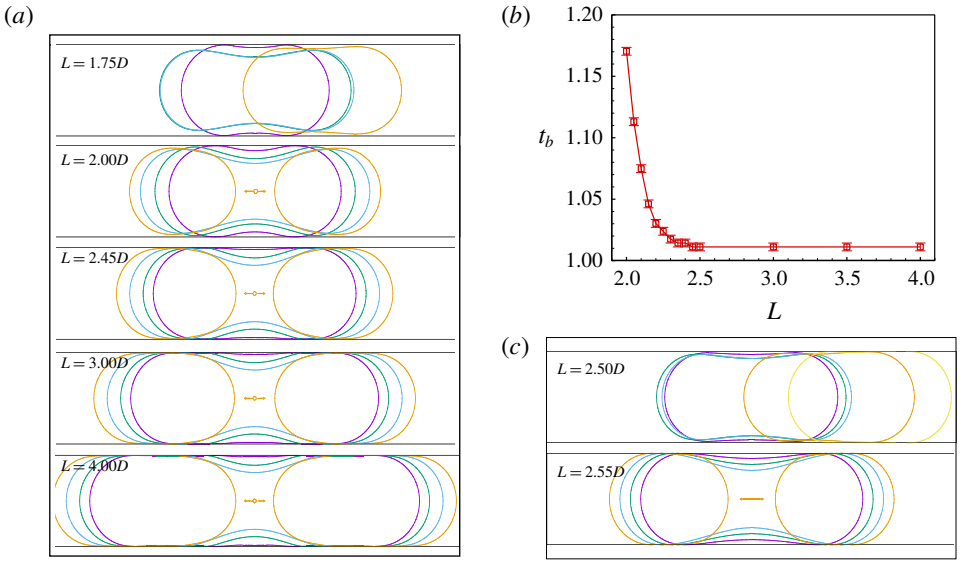


FIGURE 14. (Colour online) (*a*) Three types of droplet dynamics, non-breakup, non-obstructed breakup, and obstructed breakup, for different L under $Ca = 2.0 \times 10^{-4}$. (*b*) Evolution of the breakup time with L for $Ca = 2.0 \times 10^{-4}$. (*c*) Two types of droplet dynamics, non-breakup and obstructed breakup, for different L under $Ca = 2.0 \times 10^{-5}$.

of the neck region and the cylindrical region, as observed previously in figure 6(*b*). Figure 14(*c*) shows that the non-obstructed breakup vanishes as Ca decreases to 2.0×10^{-5}. L_{cr} for $Ca = 2.0 \times 10^{-5}$ and 2.0×10^{-6} are obtained directly from the boundary between non-breakup and obstructed breakup to be $2.53D$ and $2.68D$, respectively. L_{cr} thus increases only by approximately 10 % as Ca decreases by two orders of magnitude. This slow variation of L_{cr} with Ca is roughly in agreement with the experimental observations for droplet breakup in a T-junction (Jullien *et al.* 2009), that L_{cr} is independent of Ca (in a range between 4×10^{-4} and 2×10^{-1}). As the variation of L_{cr} with Ca is related to the non-breakup situation, the flow through the tunnel between the droplet and the wall should be considered. The flow dynamics is beyond the scope of the present paper and will be considered in a future study.

4. Concluding remarks

The present study highlights the essential role of capillarity and ultimately illuminates the two origins of capillary instability of confined fluid threads in microfluidic channels. Distinct from an unbounded fluid thread, a confined fluid thread is stabilized by its internal pressure and destabilized by the gradient of the capillary pressure induced by confinements or local capillary pressure that exceeds this internal pressure. The revealed mechanisms not only explain the underlying physics but also can be used to invent new configurations of microfluidic devices that can further improve the precision and efficiency of droplet/bubble generation.

Acknowledgements

This work was partly supported by the National Natural Science Foundation of China (grant nos 11772343, 11832017, 11572334 and 11402274), the CAS Key

https://doi.org/10.1017/jfm.2019.426 Published online by Cambridge University Press

Research Program of Frontier Sciences (QYZDB-SSW-JSC036), the CAS Strategic Priority Research Program (XDB22040403) and the Beijing Institute of Technology Research Fund Program for Young Scholars.

Supplementary movies and material

Supplementary movies and material are available at https://doi.org/10.1017/jfm.2019.426.

REFERENCES

ANNA, S. L. 2016 Droplets and bubbles in microfluidic devices. *Annu. Rev. Fluid Mech.* **48**, 285–309.

BERESNEV, I. A., LI, W. Q. & VIGIL, R. D. 2009 Condition for break-up of non-wetting fluids in sinusoidally constricted capillary channels. *Trans. Porous Med.* **80** (3), 581–604.

BHAT, P. P., APPATHURAI, S., HARRIS, M. T., PASQUALI, M., MCKINLEY, G. H. & BASARAN, O. A. 2010 Formation of beads-on-a-string structures during break-up of viscoelastic filaments. *Nat. Phys.* **6** (8), 625–631.

BLANCHETTE, F. & BIGIONI, T. P. 2006 Partial coalescence of drops at liquid interfaces. *Nat. Phys.* **2** (4), 254–257.

BRAKKE, K. A. 1992 The surface evolver. *Exp. Math.* **1** (2), 141–165.

BRETHERTON, F. P. 1961 The motion of long bubbles in tubes. *J. Fluid Mech.* **10** (2), 166–188.

CHEN, X., MA, D., YANG, V. & POPINET, S. 2013 High-fidelity simulations of impinging jet atomization. *Atomiz. Sprays* **23** (12), 1079–1101.

CHEN, X., XUE, C., ZHANG, L., HU, G., JIANG, X. & SUN, J. 2014 Inertial migration of deformable droplets in a microchannel. *Phys. Fluids* **26** (11), 112003.

CHEN, X. & YANG, V. 2014 Thickness-based adaptive mesh refinement methods for multi-phase flow simulations with thin regions. *J. Comput. Phys.* **269**, 22–39.

DANGLA, R., FRADET, E., LOPEZ, Y. & BAROUD, C. N. 2013 The physical mechanisms of step emulsification. *J. Phys.* D*: Appl. Phys.* **46** (11), 114003.

DE MENECH, M., GARSTECKI, P., JOUSSE, F. & STONE, H. A. 2008 Transition from squeezing to dripping in a microfluidic T-shaped junction. *J. Fluid Mech.* **595**, 141–161.

DELAUNAY, C. H. 1841 Sur la surface de révolution dont la courbure moyenne est constante. *J. Math. Pures Appl.* **16**, 309–314.

DOLLET, B., VAN HOEVE, W., RAVEN, J. P., MARMOTTANT, P. & VERSLUIS, M. 2008 Role of the channel geometry on the bubble pinch-off in flow-focusing devices. *Phys. Rev. Lett.* **100** (3), 034504.

DUCLAUX, V., CLANET, C. & QUERE, D. 2006 The effects of gravity on the capillary instability in tubes. *J. Fluid Mech.* **556**, 217–226.

EGGERS, J., FONTELOS, M. A., LEPPINEN, D. & SNOEIJER, J. H. 2007 Theory of the collapsing axisymmetric cavity. *Phys. Rev. Lett.* **98** (9), 094502.

EGGERS, J. & VILLERMAUX, E. 2008 Physics of liquid jets. *Rep. Prog. Phys.* **71** (3), 036601.

GARSTECKI, P., STONE, H. A. & WHITESIDES, G. M. 2005 Mechanism for flow-rate controlled breakup in confined geometries: a route to monodisperse emulsions. *Phys. Rev. Lett.* **94** (16), 164501.

GHORBANIAN, S., QASAIMEH, M. A. & JUNCKER, D. 2010 Rapid prototyping of branched microfluidics in PDMS using capillaries. http://blogs.rsc.org/chipsandtips/2010/05/03/, [Accessed 22-May-2015].

GORDILLO, J. M., SEVILLA, A., RODRIGUEZ-RODRIGUEZ, J. & MARTINEZ-BAZAN, C. 2005 Axisymmetric bubble pinch-off at high Reynolds numbers. *Phys. Rev. Lett.* **95** (19), 194501.

HOANG, D. A., PORTELA, L. M., KLEIJN, C. R., KREUTZER, M. T. & VAN STEIJN, V. 2013 Dynamics of droplet breakup in a T-junction. *J. Fluid Mech.* **717**, R4.

VAN HOEVE, W., DOLLET, B., VERSLUIS, M. & LOHSE, D. 2011 Microbubble formation and pinch-off scaling exponent in flow-focusing devices. *Phys. Fluids* **23** (9), 092001.

https://doi.org/10.1017/jfm.2019.426 Published online by Cambridge University Press

VAN HOEVE, W., GEKLE, S., SNOEIJER, J. H., VERSLUIS, M. L., BRENNER, M. P. & LOHSE, D. 2010 Breakup of diminutive Rayleigh jets. *Phys. Fluids* **22** (12), 122003.

JULLIEN, M. C., CHING, M. J. T. M., COHEN, C., MENETRIER, L. & TABELING, P. 2009 Droplet breakup in microfluidic T-junctions at small capillary numbers. *Phys. Fluids* **21** (7), 072001.

LINK, D. R., ANNA, S. L., WEITZ, D. A. & STONE, H. A. 2004 Geometrically mediated breakup of drops in microfluidic devices. *Phys. Rev. Lett.* **92** (5), 054503.

OLBRICHT, W. L. 1996 Pore-scale prototypes of multiphase flow in porous media. *Annu. Rev. Fluid Mech.* **28** (1), 187–213.

Persistence of Vision Pty. Ltd, 2013 Persistence of vision raytracer (version 3.7.0), http://www.povray.org/.

PLATEAU, J. 1873 *Experimental and Theoretical Steady State of Liquids Subjected to nothing but Molecular Forces*. Gauthiers-Villars.

POPINET, S. 2009 An accurate adaptive solver for surface-tension-driven interfacial flows. *J. Comput. Phys.* **228** (16), 5838–5866.

RAYLEIGH, LORD 1878 On the instability of jets. *Proc. Lond. Math. Soc.* **1** (1), 4–13.

ROOF, J. G. 1970 Snap-off of oil droplets in water-wet pores. *Soc. Petrol. Engng J.* **10** (1), 85–90.

SHUI, L. L., MUGELE, F., VAN DEN BERG, A. & EIJKEL, J. C. T. 2008 Geometry-controlled droplet generation in head-on microfluidic devices. *Appl. Phys. Lett.* **93** (15), 153113.

SQUIRES, T. M. & QUAKE, S. R. 2005 Microfluidics: fluid physics at the nanoliter scale. *Rev. Mod. Phys.* **77** (3), 977–1026.

VAN STEIJN, V., KLEIJN, C. R. & KREUTZER, M. T. 2009 Flows around confined bubbles and their importance in triggering pinch-off. *Phys. Rev. Lett.* **103** (21), 214501.

STONE, H. A., BENTLEY, B. J. & LEAL, L. G. 1986 An experimental study of transient effects in the breakup of viscous drops. *J. Fluid Mech.* **173**, 131–158.

TAGAWA, Y., OUDALOV, N., VISSER, C. W., PETERS, I. R., VAN DER MEER, D., SUN, C., PROSPERETTI, A. & LOHSE, D. 2012 Highly focused supersonic microjets. *Phys. Rev.* X **2** (3), 031002.

TAYLOR, G. I. 1961 Deposition of a viscous fluid on the wall of a tube. *J. Fluid Mech.* **10** (2), 161–165.

WONG, H., RADKE, C. J. & MORRIS, S. 1995 The motion of long bubbles in polygonal capillaries. Part 1. Thin films. *J. Fluid Mech.* **292**, 71–94.

https://doi.org/10.1017/jfm.2019.426 Published online by Cambridge University Press